university of groningen

University Medical Center Groningen

University of Groningen

Networks of Functional Metal Oxides Towards Neuromorphic Materials

Berg, Alexandra Irene

DOI:
10.33612/diss.697740687

IMPORTANT NOTE: You are advised to consult the publisher's version (publisher's PDF) if you wish to cite from it. Please check the document version below.

Document Version
Publisher's PDF, also known as Version of record

Publication date:
2023

Link to publication in University of Groningen/UMCG research database

Citation for published version (APA):
Berg, A. I. (2023). *Networks of Functional Metal Oxides Towards Neuromorphic Materials*. [Thesis fully internal (DIV), University of Groningen]. University of Groningen. https://doi.org/10.33612/diss.697740687

Copyright
Other than for strictly personal use, it is not permitted to download or to forward/distribute the text or part of it without the consent of the author(s) and/or copyright holder(s), unless the work is under an open content license (like Creative Commons).

The publication may also be distributed here under the terms of Article 25fa of the Dutch Copyright Act, indicated by the "Taverne" license. More information can be found on the University of Groningen website: https://www.rug.nl/library/open-access/self-archiving-pure/taverne-amendment.

Take-down policy
If you believe that this document breaches copyright please contact us providing details, and we will remove access to the work immediately and investigate your claim.

Downloaded from the University of Groningen/UMCG research database (Pure): http://www.rug.nl/research/portal. For technical reasons the number of authors shown on this cover page is limited to 10 maximum.

Download date: 24-02-2024

2
Experimental Methods and Techniques

Abstract

Here we describe the experimental methods used throughout this thesis, including both the general concepts, as well as all the concrete experimental parameters of every process. In addition, we also discuss the issues that were encountered, particularly during the synthesis process, and include practical recommendations to those planning to work in this direction.

2.1. SAMPLE FABRICATION

The samples discussed in this work are fabricated by a combination of polymer imprinting and polymer templating to obtain an interconnected network structure of metal oxides, consisting of imprinted stripes and templated lines, or 'fingerprint', structures. The advantage of polymer imprinting over photolithography is the reduced cost of fabrication: While photolithography is needed to fabricate the master pattern (usually in a silicon wafer) to be used for the polymer imprinting, the resulting master can then be used many times for stamp fabrication. This reduces the overall cost of fabrication compared to the use of photolithography as the standard method for pattern formation. Polymer templating is a bottom-up technique, in which the formation of patterns is driven by the self-assembly of a block copolymer (BCP) that generally consists of a hydrophobic and a hydrophilic block (see Chapter 3, section 3.3 for a more extensive explanation on BCP). Different designs of the BCP allow for the formation of different patterns (see section 3.3). In order to use BCPs for templating, care should be taken that the solvents are compatible with the BCP, such that they are able to infiltrate (either in the gas or liquid phase) one of the polymer blocks (typically the hydrophilic one), see also sections 3.3.1 and 3.3.2. In this thesis, either liquid infiltration or chemical solution deposition (CSD), is used and the details are given in the following subsections.

2.1.1. POLYMER IMPRINTING

Polymer imprinting is a top-down method, where a polymer stamp that is fabricated from a silicon master (obtained through lithography), is imprinted into a polymer in order to transfer the stamp pattern. When the pattern transfer is complete, the stamp is removed from the polymer film and the remaining structure can be used as a template for pattern formation with other materials. In this work, the stamps are imprinted in a spin-coated polystyrene (PS) film. In order to form the stamp, the PS film has to be heated to above its glass transition temperature ($T_g \sim 100\,°C$) [1] during the imprinting process. A 200 g load is applied to allow for the film to fully adopt the structure of the stamp. The stamp and sample are then cooled down to 40 °C such that the PS sets, after which the stamp is removed and the pattern is successfully transferred to the PS film. In order to use the imprinted sample for spin coating of the metal oxide precursor solution, it is treated by either O_2-plasma, or UV-ozone cleaning in order to make the surface hydrophilic, such that the precursor solution wets the structure properly. Then the precursor solution is spin coated onto the imprinted PS and incorporated in the imprinted pattern by capillary action. The sample is thermally treated to oxidize and crystallize the metal oxide and to remove the polymer template, resulting in a metal oxide nanostructure (Figure 2.1).

In this work we have used silicon masters with a grating pattern, but different shapes such as cylinders can be used as well. [2] In order for the stamp to be reusable, it has to be made from a material that is flexible enough to be peeled off the imprinted material, but hard enough not to collapse, break, or degrade after only a few uses. Poly(dimethylsiloxane) (PDMS) is a material that meets these criteria and is, therefore, a popular material to be used for polymer stamps. However, care should be taken in selecting PDMS with the right material properties to be able to pattern sub-100 nm structures without stamp deformation. When the

Figure 2.1 | Schematic overview of the sample fabrication steps in polymer imprinting. A PS film is spin coated on a silicon wafer and a PDMS stamp is applied to the film (1) under a load of 200 g at a temperature of 150 °C. Once the imprinting is finished, and the sample has cooled down to well below the glass transition temperature of PS, the PDMS stamp is removed and the PS film shows the imprinted structure (2). Using spin coating, the metal oxide precursor solution is loaded into the imprinted film (3) and subsequent thermal annealing results in the oxidation of the metal oxide precursor and the removal of the polymer matrix, leaving a metal oxide nanostructure (4).

PDMS is too soft, the stamps will deform through buckling and small features on the patterns will collapse,[3] preventing reliable pattern transfer and reducing the stamp lifetime to only one or a few uses. This is an issue that arises with the most commonly used PDMS (Sylgard 184), which has a low elastic modulus (2.0 N/mm^2),[3] resulting in easy stamp deformation, preventing patterning at scales below 500 nm. These deformation issues can be resolved by using a PDMS with a higher elastic modulus: h-PDMS (~9 N/mm^2), resulting in better structure preservation over long-term stamp usage and allowing for the use of PDMS stamps for patterning features at sub-100 nm scale. However, using only *h*-PDMS causes the stamps to be too inflexible, resulting in cracking of the stamps in the stamp fabrication process. Therefore, composite stamps consisting of two layers are used, using the best features of both *h*-PDMS and the softer Sylgard-184 PDMS. In the composite stamps, a thin layer of the stiff *h*-PDMS holds the pattern and it is supported by a thick (cushion) layer of soft PDMS giving the stamp the desired flexibility for handling.[3]

EXPERIMENTAL DETAILS ON POLYMER IMPRINTING

Polymer imprinting: A 2 wt% solution of polystyrene (PS, Polymer Source, Mw/Mn = 1.04) in toluene was aged overnight. The solution was filtered using a PTFE 0.20 µL syringe filter before spin coating (Polos SPIN 150i) on the cleaned Si substrates (section 2.1.3) at 3600 rpm for 30 s. The sample was preheated to 90 °C on a hotplate and the PDMS stamp was pressed onto the PS film with a 200 g load. The temperature was increased to 150 °C for 20 min, after which the setup was cooled naturally to 40 °C and the stamp was removed from the sample. The imprinted samples were treated by O_2-plasma cleaning (Harrick Plasma PDC-002) for 30 s or UV/O_3 (Ossila) cleaning for 5 min, before metal oxide precursor deposition by spin coating at 3500 rpm for 60 s. The samples were thermally treated in a box furnace (Nabertherm) under ambient atmosphere for the samples discussed in chapter 4, or in a tube furnace (Nabertherm) under constant oxygen flow (300 cc/min), for the samples discussed in chapter 5, to form the metal oxide nanostructures.

PDMS stamp fabrication: Silicon masters for the PDMS stamp fabrication were obtained from Eulitha (NIL Imprint Stamps, MP300L600 Multi-period linear gratings). With specified line width/ periods (±10 %) of 140/300, 215/400, 260/500, and 320/600 nm and a line height of 180 nm ±10 %. The method for fabrication of composite PDMS stamps was adapted from Odom et al.[3] The materials for the PDMS fabrication were purchased from abcr GmbH. The vinyl prepolymer ((7.0-8.0 % vinylmethylsiloxne)-dimehtylsiloxane copolymer, VDT-731, 3.4 g) was mixed with the Pt catalyst (platinum divinyltetramethyldisiloxane, 18 µL) and

Figure 2.2 | a) Chemical structure of PS-*b*-P2VP and b) a schematic overview of the sample fabrication steps for polymer templating. The BCP film is spin coated on a silicon wafer and undergoes self-assembly during the solvent vapor annealing (SVA) step in chloroform (1). In order to allow for the inclusion of the metal oxide precursor solution, the sample undergoes a second SVA step in ethanol to swell and allow for metal ion inclusion into the P2VP block by spin coating (2). Subsequent UV-ozone treatment and thermal annealing results in the oxidation of the metal oxide precursor and the removal of the polymer matrix, leaving a metal oxide nanostructure (3).

the modulator (2,4,6,8-tetramethyltetravinylcyclotetrasiloxane, 50 µL) and degassed for 2-10 min, or until bubbles were no longer present. The hydrosilane prepolymer ((25-35 % methylhydrosyloxane)-dimethylsiloxane copolymer, HMS-301, 1.08 g) was gently mixed in as to not introduce new bubbles. The masters were coated with the resin and left to fill the pattern for 5 min before spin coating at 2000 rpm for 40 s at a 1000 rpm/s ramp rate after which they were cured at 60 °C for 30 min. Sylgard 184 (Sigma Aldrich) cushions were fabricated beforehand (resin:crosslinker ratio = (10-10.1):1) and were cut and glued to the h-PDMS stamps using the h-PDMS resin and cured for 2 h at 60 °C. The stamps were peeled off the masters while still warm, and excess PDMS around the imprinted area was removed by cutting using a sharp razor blade.

2.1.2. BLOCK COPOLYMER TEMPLATING

In this work a polystyrene-*block*-poly(2-vinylpyridine) (PS-*b*-P2VP) block copolymer was used with near-equal block sizes (Figure 2.2a), that self-assembles in vertical lamellae. The metal oxides were templated by chemical solution deposition (CSD). For the PS-*b*-P2VP, the metal oxide inclusion operates on the basis that the PS block is hydrophobic, while the P2VP block is hydrophilic. The nitrogen in the pyridine ring coordinates to the metal ions in the precursor solution, allowing for inclusion into the P2VP block. After the initial spin coating of the polymer film, the desired morphology is not yet obtained, while the overall structure already hints to a lamellar morphology, the self-assembly has not completed yet. Solvent vapor annealing (SVA) is used to complete the self-assembly in a controlled environment. During SVA, the sample is enclosed in a container, together with a vial of the solvent that dissolves the polymer. The container is then closed and heated at a constant temperature, chosen in such a way that the solvent evaporates slightly to create a vapor pressure in the container. This solvent vapor pressure enhances the polymer chain mobility in the film, allowing for self-assembly of the BCP. The samples are then treated with a second SVA step in order to swell the P2VP blocks to allow for easier incorporation of the metal ions during spin coating. The solvent for the second SVA should be chosen such that it will only swell the hydrophilic block and not mobilize the polymer chains again. Finally, the samples are treated by ozone cleaning in order to oxidize the nanostructures and remove the polymer template, such that only the metal oxide nanostructure remains on the sample surface (Figure 2.2).

In this thesis, polymer imprinting and polymer templating are combined in order to create interconnected network structures of various different metal oxides (Chapter 4 and 5). Additionally, stacking multiple imprinted and/ or templated layers allows for the formation of 3D networks (Chapter 5).

EXPERIMENTAL DETAILS - AND DISCUSSION - POLYMER TEMPLATING

15 mg/mL (Chapter 4) or 10 mg/mL (Chapter 5) polystyrene-block-poly(2-vinylpyridine) (Polymer Source, Mw/Mn = 1.15, Mn PS(133 000) – P2VP(132 000)) solutions in chloroform were aged overnight at room temperature, under gentle stirring at 100 rpm. The aged solutions were filtered using a PTFE 0.20 µL syringe filter before spin coating (3500 rpm, 30 s) on either bare silicon wafers or previously imprinted samples. Solvent vapor annealing (SVA) was performed to promote the self-assembly of the block copolymer chains. The SVA was performed in a closed 50 mL bottle containing the sample and a 4 mL vial filled with 2 mL chloroform, which was placed in an oven set to a constant temperature close to room temperature (26-28 °C) and annealed overnight. A second SVA step (3 mL ethanol (abs.), 50 °C, 20 min) was performed to swell the P2VP block, allowing for the metal oxide precursor loading. After the second SVA, the sample was cooled to room temperature before spin coating the metal oxide precursors. The coated samples were treated by UV ozone (Novascan PSDP UV ozone cleaner) for 210 min (stage temperature 22 °C) to oxidize the material and remove part of the polymer template.[4] Thermal annealing followed to fully oxidize the networks and remove the polymer template.

While the method for the BCP templating looks quite simple and straightforward on paper, there are a few experimental caveats that came to light during the course of this project. Following is a discussion on these encountered issues with possible solutions, workarounds, and important experimental cues that should be taken into account.

Firstly, the temperature in the lab is an important parameter when working with volatile solvents and can have a great impact on the quality of the BCP solution and the final structure of the self-assembled BCP films. Since the solvent for PS-*b*-P2VP is chloroform, which is volatile and easily evaporates at room temperature, temperature fluctuations in the lab (especially in summer time) can cause the solvent to evaporate even faster than usual. This then affects the aging of the BCP solution and, ultimately, also the self-assembly of the BCP.

Initially, a BCP solution with a concentration of 15 mg/mL was used (Chapter 4). However, the result of the BCP self assembly and resulting film morphology was difficult to reproduce, and would often result in the absence of (long-range) fingerprint formation, even up to a point where the lamellar morphology could not be obtained for months. As mentioned above, this issue was especially noticeable in the warmer months (Figure 2.3). The correct morphology was only obtained consistently again after lowering the concentration of the BCP solution to 10 mg/mL (Chapter 5). We hypothesize that the lab temperature is the key factor here. With faster evaporation of the solvent, the BCP solution will effectively get a higher concentration, giving rise to a higher thickness. Since BCP self-assembly is strongly dependent on film thickness and favorable surface energies,[5–8] thicker films will result in different sample morphologies(i.e., formation of horizontal lamellae instead of vertical ones). In the case of the 10 mg/mL solution, the success rate might be higher due to a wider available margin until

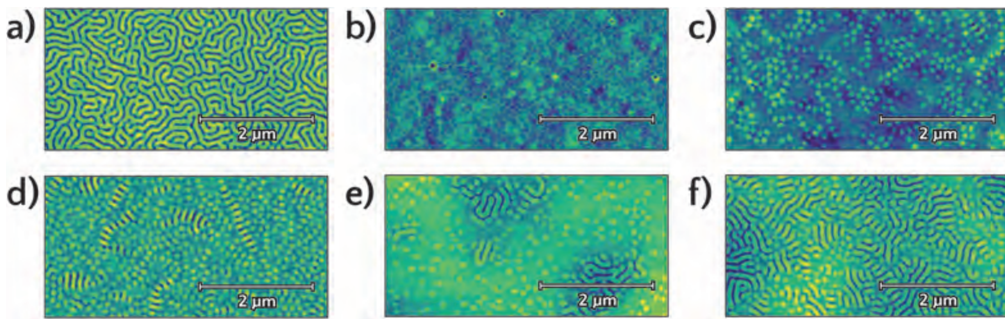

Figure 2.3 | Overview of different surface morphologies observed for the BCP self-assembly. Firstly, the desired 'fingerprint' morphology (a), with long-range connectivity of vertical lamellae. Following are some of the observed morphologies lacking the long-range fingerprint structure: a mostly flat surface with no clear features (apart from a few holes in the polymer film) (b); a sparse collection of cylindrical (dot-like) structures (c); a dense collection of cylinders, with some small areas of short-range lamellar structures (d); large areas of cylindrical shapes with small patches of lamellar morphology (e); and finally, a mix of mid- to long-range lamellar morphologies intersected by cylindrical and short-range lamellar morphologies (f).

reaching a 'critical concentration' at which lamella formation is no longer favorable. While this is postulated to be the main cause of the self-assembly and morphology issues in the samples, solid evidence is lacking.

Additionally, once spin coated, the chloroform can readily evaporate from the thin film in the time span between finishing the spin coating and starting the SVA process. We hypothesise that evaporation of the solvent forms a dry 'skin', capping the film, with (very) limited mobility of the polymer chains, preventing the self-assembly into the lamellar morphology in at least the top layer. In many of the cases in which the lamellae were not successfully formed, the morphology was either fully flat (no structure) or showed spherical/cylindrical patterns in varying densities/sparsity (2.3). There were no indications that this effect was reversible once the sample was exposed to chloroform vapor during the SVA process.

To those planning to reproduce these results, it may be useful to mention that a visual indication of correct film thickness is a blue color to the film. It should be noted that the type of silicon wafer can influence the perceived film color. The intrinsic Si wafers that were used in this project already have a blue tint, whereas the n-doped Si wafers are more towards black. However, in both cases a blue hue was observed for BCP samples with the desired lamellar morphology; while films that lack the lamellar morphology show a brown hue.

It is also recommended to make a new BCP solution every time before use, especially in the warmer months, to prevent the BCP stock from changing too rapidly in concentration and drastically lowering the success rate of obtaining lamellar morphologies with long-range order, since even storing the stock in the fridge does not counteract the evaporation successfully. However, when the lab temperatures are lower (around 22 °C), the BCP stock can actually be used for a few weeks, as long as it is stored in the fridge in between uses.

Ideally, these fabrication steps should be performed in a lab with proper temperature control, well below ~25 °C. Alternatively, the concentration of the BCP solution could be adjusted accordingly.

2.1.3. SUBSTRATE PREPARATION

As mentioned before, silicon wafers were used as a substrate in this work. While silicon with different doping have been used, all of the substrates were cut from one-side-polished Si(100) (Sil'tronix) wafers to substrates of approximately 1x1 cm^2. A cleaning procedure was developed for the cut substrates to clean any dust, particles, or residual contamination resulting from wafer handling, in order to prevent film inhomogeneities during spin coating and allow for proper wetting of the polymers on the substrate. Initially, the cut substrates were cleaned with pressurized air to remove any large particles on the surface. Then, the substrates were cleaned by 10 min UV-ozone (UV/O_3) treatment to remove any organic contaminants, followed by ultrasonication in acetone (10 min) and ethanol (10 min). After ultrasonication, the substrates were blow-dried with pressurized air and treated with a final UV/O_3 cleaning step (10 min). The final UV/O_3 steps removes organic residue from the cleaning procedure. Additionally, UV/O_3 treatment increases the hydrophilicity of the substrate surface, allowing for proper wetting of the polymer films during spin coating. For this reason, it is important to proceed with the polymer spin coating as soon as possible, preferably within 10 min after finishing the UV/O_3 treatment.

2.2. ATOMIC FORCE MICROSCOPY TECHNIQUES

Atomic Force Microscopy (AFM) is a great (and readily available) tool to image the surface of samples, allowing for a variety of imaging modes, from imaging the surface topography, to measuring magnetic properties (MFM), piezoelectric properties (PFM), and electrical properties (cAFM, KPFM), only to name a few.

AFM operates on the principle of a small spring-like cantilever, with a sharp tip (with a radius ranging between 10-30 nm for a pristine tip), that is oscillated by a piezo stack wile it scans over the surface of a sample. The cantilever displacement is tracked using a laser that is reflected off the cantilever onto a photodiode, and translated to an image of the surface topography. There are two modes of operation in AFM: contact-mode (CM) AFM and tapping-mode (TM) AFM. In CM-AFM, the tip is brought into direct contact with the sample surface, and the tip-sample force is kept constant during scanning through a feedback loop: changes in the cantilever deflection, due to surface topography, cause the feedback loop to adjust the height at which the cantilever is scanned over the surface to keep the force constant. These height changes then result in the final topography image of the sample. It should be noted that CM-AFM can be damaging to the sample, especially softer samples, and the tip, wearing off tip coatings and dulling the sharpness of the tip, especially when the samples exhibit a large surface roughness. In TM-AFM the tip oscillates near its resonance frequency above the sample surface, and only contacts the sample surface a fraction of the time it takes to complete the scan.[9–11] Using a feedback loop, the tip oscillation frequency is kept constant, since the oscillation frequency is influenced by proximity to the surface due to electrostatic interactions between the tip and sample surface. TM-AFM is generally less damaging to the tip and sample compared to CM-AFM, and is therefore often the mode of choice for general surface imaging. In this work, TM-AFM was used for the standard topography imaging of the samples.

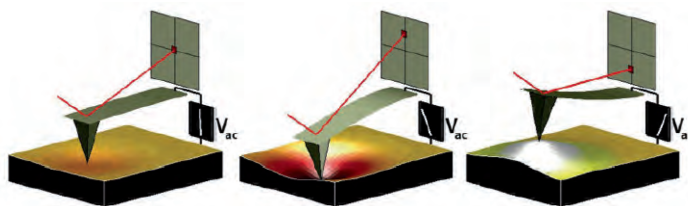

Figure 2.4 | Schematic of PFM operation. The sample deforms as a response to the applied voltage, This causes the cantilever to deflect. The deflection can then be measured and interpreted in terms of the piezoelectric properties of the sample. Reprinted from Proksch and Kalinin, Asylum Research PFM Application Note (2008). [13]

PFM is a contact mode technique which allows the user to measure both topography and electromechanical deformation of piezoelectric samples. This is done by applying a voltage to the sample through the AFM tip. An AC voltage is applied to the tip, which is then scanned across the surface. The amplitude of tip deflection depends on the strength of the electromechanical coupling between the tip and the sample, and contains information on the polarization direction of the piezoelectric domains, with respect to the applied bias (Figure 2.4). The signals of the driving voltage and piezoresponse are in phase when the polarization is in the same direction as the applied bias, while the signals will be out of phase for opposite polarization directions. In the case of so-called Vector PFM, both the vertical deflection of the cantilever, as well as its lateral torsion are recorded, therefore imaging both the in-plane and the out-of-plane components of the piezoelectric deformation. [12,13] It should be noted that quantification of piezoelectric effect using PFM is difficult and remains an issue in the scientific community. [14,15] Topography cross-talk, electrostatic, and mechanical effects (such as oxygen migration under applied bias) are difficult to disentangle from an intrinsic electromechanical signal. Therefore, PFM measurements can be used for an indication of trends and piezoelectric behavior in samples, but additional measurement techniques should be used to support a claim of the piezoelectric nature of a given sample.

In cAFM, the topography and current across the sample are simultaneously recorded in a contact mode operation. For current sensing, the tip needs to be conductive. This is generally achieved through a conductive coating on a Si cantilever, or a fully metallic probe. A voltage has to be applied to create a potential difference between the tip and the sample. The tip-sample contact quality is important for cAFM, since the recorded current depends on the effective area of the contact as $I = J \times A_{eff}$, where J is the current density and A_{eff} the effective contact area. It should be, therefore, also noted that tip-wear is an issue that is significant in cAFM measurements, since it will affect the contact area and the amount of current that can be recorded by the tip. It is, therefore, important that the right conductive tips are selected for each sample to minimize tip degradation.

An advantage of AFM over other microscopy techniques is that a 3D imaging of the sample surface is easily obtained. Additionally, information is easily accessible, such as mechanical properties and phase images. While the scanning speed greatly depends on the sample, the overall process of performing AFM measurements is fast (for standard measurements in ambient conditions, for which no special sample preparation is required). However,

there are also some disadvantages of AFM techniques that should be pointed out. The imaged area is relatively small, with maximum scan ranges between 20-90 µm for most AFM systems, so multiple locations should be imaged on the sample to give an indication of sample homogeneity. Next, artifacts can arise in the image due to tip effects: streaking can arise from tip drag along features in the scanning direction, a dirty tip can causes apparent features that are not actually on the sample. Thermal drift is often an issue when scanning at or above room temperature, and due to tip shape and dimensions, steep walls or overhangs cannot be imaged properly.

The AFM data presented in this thesis was obtained using two AFM setups. The general topography imaging was performed using a Bruker Dimension Icon. PFM and cAFM measurements were performed using an Asylum Research Cypher ES.

2.3. X-RAY PHOTOELECTRON SPECTROSCOPY

X-ray photoelectron spectroscopy (XPS) is a non-destructive, surface sensitive characterization technique for chemical analysis, based on the photoelectric effect. In XPS, the sample is irradiated by a, preferably, monochromatic X-ray beam, typically using Mg Kα (1253.6 eV) or Al Kα (1486.6 eV) radiation. These X-ray photons interact with atoms in the surface layers of the sample and cause electrons to be emitted via the photoelectric effect: the electrons are emitted at specific energies, depending on the atomic orbital they are emitted from, and are analyzed as a function of their kinetic energy. The kinetic energy of the electrons can be calculated as:

$$KE = h\nu - BE - \phi_s \tag{2.1}$$

Where KE is the kinetic energy, hν is the photon energy, BE is the binding energy of the atomic orbital, and ϕ_s is the spectrometer work function.

Each element has a unique set of electron binding energies and, therefore, a unique XPS spectrum. Since the peak intensity is directly related to abundance of the element in the probed sample volume, this information can be used to quantify the sample stoichiometry. In order to quantify atomic ratios, the fitted peak areas are divided by an atomic sensitivity factor (ASF). This is an empirically derived factor that is different for each element and depend on both atomic properties and experimental parameters specific to the system used (see also section 2.3.1).

Next to quantification of the elements in the sample, information on the chemical state of the elements can be obtained from the XPS spectrum. Depending on the chemical environment, the binding energy of the electrons is influenced (due to changes in chemical potential and polarizability of compounds), resulting in a chemical shift, with respect to the pure element state, when elements are bonded to other elements. Additionally, information on the oxidation state of elements can be obtained. Different formal oxidation states change the chemical shift of the peaks and the presence of multiple peaks can indicate a coexistence of multiple oxidation states within the sample. The reader is referred to the books by Moulder et al.[16] and Vickermanet al.[17] for a more in-depth introduction to XPS.

Peak fitting in XPS requires a mixture of scientific knowledge and experience, as the XPS data are prone to overfitting and misinterpretation. Additionally, peak shapes and

splitting can be caused by both the sample and instrument settings. Therefore, peak fitting should be done with care: included peaks should make sense (chemically) and realistic peak relationships should be taken into account.[16,17] For example, when fitting a peak that shows a peak degeneracy due to electrons from a degenerate orbital (p, d, f), the peak splitting and peak intensity ratios are known and can be added as a constraint in the fit. Additionally, typical ranges of full-width-half-maximum (FWHM) for peaks in different materials are known and should be taken into account when fitting.[16]

2.3.1. REDEFINING THE ATOMIC SENSITIVITY FACTOR

The ASFs are empirically derived factors that are used to normalize the peak intensity in order to obtain atomic concentrations of the elements. The ASF are given by:

$$I = n\sigma DJL\lambda AT \tag{2.2}$$

Where I is the atomic sensitivity factor, n is the number of atoms of the element per cm^3, σ is the photoelectric cross-section of the atomic orbital in cm^2, D is the detection efficiency of the emitted electrons, J is the X-ray flux of photons/$cm^2 \cdot s$, L is the orbital angular symmetry function, λ is the electron mean free path, A is the sample area in cm^2, and T is the transmission coefficient.

The ASFs are tabulated for two source-detector angles (90°, 54.7°).[16] However, the setup used for XPS measurements in this thesis has a source-detector angle of 30°, which is significantly different from the tabulated values, requiring a recalculation of the ASFs to prevent large uncertainties in the results.

The only angle-dependent variable in equation 2.2 is the orbital angular symmetry function (L):

$$L = 1 + \beta(3sin^2(\theta/2) - 1)/2 \tag{2.3}$$

Where β is the element sub-shell constant (X-ray dependent) and θ the source-detector angle in degrees. β can be obtained by equating the ASFs for the detector angles at 90° and 54.7°. Then, this value can be used to extrapolate the ASF for the source-detector angle of 30°.

Overall, the recalculated ASFs are in general a factor 1.1-1.2 larger than the values tabulated at 54.7°. The ASFs were recalculated for the XPS studies presented in this thesis and these new values were used to determine sample compositions (see Table 2.1).

2.4. X-RAY DIFFRACTION TECHNIQUES

X-ray diffraction (XRD) is a technique that allows for the determination of crystallographic phase, crystalinity, lattice parameters, and particle size. For bulk samples, single crystal XRD or powder XRD are most commonly used. In powder diffraction, the angle of the incident beam and diffracted beam are typically kept equal (Bragg-Brentano geometry) and the source and detector move in sync to detect the specular reflections of the pellet that contains a large number of randomly oriented crystallites. Intensity will be detected when the incident and

Ti 2p	**ASF**	**Bi 4f**	**ASF**	**O 1s**	**ASF**
90°	1.798	90°	7.632	90°	0.711
54.7°	2.001	54.7°	9.14	54.7°	0.711
30°	2.25	30°	11.03	30°	0.711
Sr 3d		**Fe 2p**		**Hf 4f**	
90°	1.578	90°	2.686	90°	2.221
54.7°	1.843	54.7°	2.957	54.7°	2.639
30°	2.18	30°	3.3	30°	3.16
La 3d		**Ca 2p**		**Mn 2p**	
90°	7.708	90°	1.634	90°	2.42
54.7°	9.122	54.7°	1.833	54.7°	2.659
30°	10.89	30°	2.08	30°	3.18

Table 2.1 | Recalculated atomic sensitivity factors (ASF) for the elements used in XPS quantification in this thesis (Chapter 4).

diffracted beam interfere constructively. However, this setup is not suitable for the characterization of thin films, due to the penetration depth of the X-rays into the sample. Since the films are so thin, the signal will be dominated by the substrate signal and the information of the thin film will be below the sensitivity of the technique. Typical measurement modes for thin film XRD are: 2theta/omega scans, X-ray reflectivity (XRR), reciprocal space mapping (RSM), pole figures, and grazing incidence XRD (GIXRD). In order to perform proper GIXRD, the incoming X-ray beam is kept at an incident angle below the critical angle for total reflection, such that there are no x-rays penetrating the material with a scattering vector perpendicular to the sample surface. In this way, no substrate signal is measured and the film in-plane Bragg reflections, free from the broadening typical in thin layers, are accessed. However, since this mode fully relies on the very weak and exponentially decaying evanescence wave, the diffracted intensity is weak and it mostly requires synchrotron experiments, being only useful in the case of single crystal layers. However, it is increasingly common to refer as GIXRD to the mode in which the incident angle is kept fixed to a small value, in order to minimize the substrate signal, resulting in a large sample illumination and shallow penetration depth, while the detector is scanned to collect the diffracted X-ray beams. Contrary to the previous case, this mode is useful in the case of polycrystalline films, since it gives access to those crystals that are not epitaxially oriented with the substrate.[18] Other grazing-incidence based x-ray techniques, more suitable for the work in this thesis, are Grazing Incidence Small- and Wide Angle Scattering (GISAXS and GIWAXS). More details on these methods can be found in a separate subsection below.

These methods allow for the characterization of the crystal phase, lattice parameters, film texture, film strain, and film thickness. Since these measurements are performed in reflection geometry, and the out-of-plane diffraction component is collected, a sufficient measurement volume, or film thickness, is required in order to get a good signal-to-noise ratio. In case of XRR, surface roughness also plays a role as in order to obtain the right interference conditions, the beams reflecting at the different interfaces need to be parallel to each other

and that requires the sample surface and interface with the substrate to be flat. In the case of GIXRD, surface roughness is also an issue as in that case the critical angle for total reflection is not well-defined. In polycrystalline films, grain sizes are important factors as well, as peak broadening arises at small grain sizes, according to the Scherrer equation:

$$t = \frac{K\lambda}{\beta cos(\theta)} \tag{2.4}$$

where t is the mean size of ordered crystalline domains, K is the shape factor; dimensionless and close to unity, typically equal to 0.9, but depends on the crystallite shape, λ is the X-ray wavelength, β is the peak broadening at full width half maximum (FWHM), and θ is the Bragg angle, both in radians.

In the case of the metal oxide networks discussed in this thesis, these techniques cannot be used because of the reasons listed previously. Since the films are nanostructured, not continuous, and exhibit high surface roughness, the signal intensity is too low for either bulk or thin film XRD, resulting in a very poor signal-to-noise ratio. In the case of GIXRD, the signal from the sample is high enough to distinguish peaks. However, the nanostructured surface results in extreme peak broadening, where a peak can span up to about 20°, preventing phase identification.

For the work presented in this thesis, powder XRD has been used to optimize the annealing parameters for the different materials. Since the same issues remain for the nanostructured samples, multilayered spin-coated and drop-casted films were used for the characterization by powder XRD. But other techniques had to be used to characterize the structures of the nanostructured samples.

The reader is referred to the books by Cullity and Als-Nielsen, and the Rigaku Journal paper by Shintaro Kobayashi on in-plane XRD measurements in thin films for more in-depth theory on XRD.[18–20]

2.4.1. GRAZING INCIDENCE X-RAY SCATTERING

As mentioned in the previous section, standard thin film XRD methods are not suitable for the types of samples discussed in this thesis, due to the limited diffraction volume and high surface roughness. Grazing incidence small- and wide angle scattering (GISAXS and GIWAXS) are used as an alternative to XRD in chapter 4, since they are very sensitive to thin films (well below 1 µm) and probe not only the vertical (q_z) direction, but the in-plane (q_x, q_y) directions as well. Note that q_x is negligible for GISAXS,[21,22] but should be taken into consideration for GIWAXS measurements. The scattering vectors $q_{x,y,z}$ are defined as:

$$q = \begin{cases} q_x = \dfrac{2\pi}{\lambda}\left(\cos(2\theta_f)\cos(\alpha_f) - \cos(\alpha_i)\right) \\ q_y = \dfrac{2\pi}{\lambda}\left(\sin(2\theta_f)\cos(\alpha_f)\right) \\ q_z = \dfrac{2\pi}{\lambda}\left(\sin(\alpha_i) + \sin(\alpha_f)\right) \end{cases} \tag{2.5}$$

where $2\theta_f$ is the in-plane scattering angle, α_f is the out-of-plane scattering angle, and α_i is the incident angle. In general, for thin films the configuration is used where the incidence

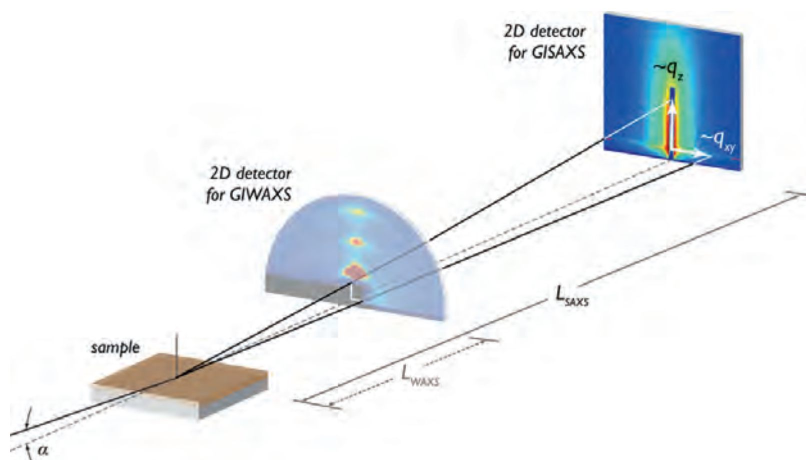

Figure 2.5 | Schematic measurement configuration for GISAXS in comparison to GIWAXS indicating the difference in sample to detector difference, with typical L_{WAXS} ~ 0.1-1 m and L_{SAXS} ~ 1-7 m. Reprinted with permission from Rivnay et al. Chem. Rev. **112**, 5488-5519 (2012).[26] Copyright 2012, American Chemical Society

angle (α_i) is very close to the critical angle (α_c), in order to maximize the film signal and minimise the scattering form the background. These techniques can be used to study surfaces and interfaces of crystalline and non-crystalline materials and buried internal structures, and are often used to investigate thin films of polymers and conjugated molecules.[23]

GISAXS and GIWAXS are closely related, with the main difference between the two methods being the range of scattering angles that are collected during the measurements and, as a result the length scales that are probed. GISAXS probes features such as size, shape, pore size, and other characteristic distances of (partially) ordered materials on the 0.5-100 nm length scale.[23–25] Since the probed length scales are (relatively) large, the scattering angles are small (0.1-10°) and a large sample to detector distance, in the order of several meters, is required to collect the scattering signals properly. GIWAXS probes atomic and molecular distances and provides information on crystal structure, atomic positions, unit cell dimensions, and crystallite size. Since the probed length scales are so small, the scattering angles are much larger compared to GISAXS, up to about 30-45°, and much smaller sample to detector distances, in the order of several centimeters up to about a meter, are required for GISAXS measurements (Figure. 2.5).[23,25]

Features from small angle X-ray scattering (providing information on lateral film structure) and diffuse X-ray reflectivity (providing information on the normal density profile) are combined for GISAXS and GIWAXS. Using a 2D detector allows for the collection of the scattering signal from the in-plane and out-of-plane driections all at once. The scattering intensity pattern of both GISAXS and GIWAXS depends on sample morphology and observed features in the spectra provide information on the sample structure (Figure 2.6, 2.7).

GIWAXS is closely related to GIXRD with the main difference between the techniques originates in the collection strategy: as mentioned before, a 2D area detector is used for GIWAXS measurements, while a point or line detector is generally used for GIXRD. The

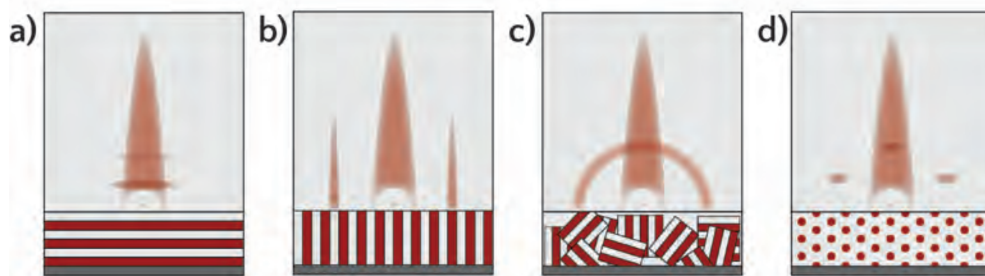

Figure 2.6 | GISAXS scattering intensity signatures based on sample morphology: a) ordered parallel lamellae, b) ordered perpendicular lamellae, c) disordered surface layers, and d) oriented thin films. Adapted from Anton Paar.[27]

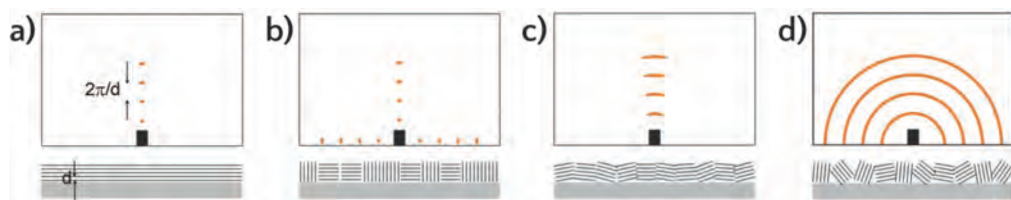

Figure 2.7 | Schematic representation of GIWAXS scattering intensity patterns based on different sample morphologies: a) horizontal lamellae, b) crystallites with mixed horizontal and vertical lamellar stacking, c) oriented crystal domains with horizontal lamellae, and d) fully disordered crystallites. Adapted with permission from Müller-Buschbaum, Adv. Mater., **26**, 7692-7709 (2014).[28] Copyright 2014, Wiley-VCH.

resolution and angles that can be detected in GIXRD are better compared to GIWAXS, but the latter measurements with the 2D detector allow for a shorter collection time. GIWAXS measurements are more appropriate for partially ordered or disordered materials, while GIXRD is more appropriate for samples with sharp diffraction peaks.[23]

2

REFERENCES

[1] J. Rieger, Journal of Thermal Analysis **46**, 965 (1996).

[2] J. Xu, *Polymer-templated chemical solution deposition of ferrimagnetic nanoarrays and multiferroic nanocomposite thin films*, Phd thesis, University of Groningen (2020).

[3] T. W. Odom, J. C. Love, D. B. Wolfe, K. E. Paul, and G. M. Whitesides, Langmuir **18**, 5314 (2002).

[4] J. Xu, J. Varghese, G. Portale, A. Longo, J. Momand, A. Syari'ati, J. A. Heuver, P. Rudolf, B. J. Kooi, B. Noheda, and K. Loos, Polymers **11**, 1598 (2019).

[5] T. Ghoshal, M. T. Shaw, C. T. Bolger, J. D. Holmes, and M. A. Morris, Journal of Materials Chemistry **22**, 12083 (2012).

[6] T. Ghoshal, T. Maity, J. F. Godsell, S. Roy, and M. A. Morris, Adv. Mater. **24**, 2390 (2012).

[7] P. W. Majewski and K. G. Yager, Journal of Physics Condensed Matter **28** (2016).

[8] J. Xu, A. I. Berg, B. Noheda, and K. Loos, Journal of Applied Physics **128**, 190903 (2020).

[9] C. Möller, M. Allen, V. Elings, A. Engel, and D. J. Müller, Biophysical Journal **77**, 1150 (1999).

[10] H. Hölscher, *AFM, Tapping Mode,* in *Encyclopedia of Nanotechnology*, edited by B. Bhushan (Springer Netherlands, Dordrecht, 2012) pp. 99–99.

[11] A. Belianinov, S. V. Kalinin, and S. Jesse, Nature Communications **6**, 6550 (2015).

[12] S. V. Kalinin, B. J. Rodriguez, S. Jesse, J. Shin, A. P. Baddorf, P. Gupta, H. Jain, D. B. Williams, and A. Gruverman, Microscopy and Microanalysis **12**, 206 (2006).

[13] R. Proksch and S. Kalinin, PFM Application Note (2008).

[14] R. K. Vasudevan, N. Balke, P. Maksymovych, S. Jesse, and S. V. Kalinin, Applied Physics Reviews **4** (2017), arXiv:1701.01128 .

[15] A. Gruverman, M. Alexe, and D. Meier, Nature Communications **10**, 1 (2019).

[16] J. F. Moulder, W. F. Stickle, P. E. Sobol, and K. D. Bomben, *Handbook of X-Ray Photoelectron Spectroscopy* (Perkin-Elmer Corporation, 1992).

[17] J. C. Vickerman and I. S. Gilmore, *Surface Analysis– The Principal Techniques*, edited by J. C. Vickerman and I. S. Gilmore (Wiley, 2009).

[18] S. Kobayashi, The Rigaku Journal **26** (2010).

[19] B. Cullity, *Elements of x-ray diffraction*, 2nd ed. (Addison-Wesley Publishing Company, 1978).

[20] J. Als-Nielsen and D. McMorrow, *Elements of Modern X-ray Physics* (Wiley, 2011).

[21] G. Santoro and S. Yu, *Grazing Incidence Small Angle X-Ray Scattering as a Tool for In-Situ Time-Resolved Studies,* in *X-ray Scattering* (InTech, 2017).

[22] J. Liu and K. G. Yager, IUCrJ **5**, 737 (2018).

[23] D. Smilgies, *GISAXS and GIWAXS,* .

[24] A. Ogi and K. Inaba, The Rigaku Journal **27**, 1 (2011).

[25] V. Abhilash, N. Rajender, and K. Suresh, *Spectroscopy of Polymer Nanocomposites* (Elsevier Inc., 2016) pp. 410–451.

[26] J. Rivnay, S. C. B. Mannsfeld, C. E. Miller, A. Salleo, and M. F. Toney, Chemical Reviews **112**, 5488 (2012).

[27] Anton Paar, *Grazing-incidence small-angle X-ray scattering (GISAXS),* .

[28] P. Müller-Buschbaum, Advanced Materials **26**, 7692 (2014).